Astron. Astrophys. 227, 294–300 (1990)

ASTRONOMY AND ASTROPHYSICS

The ESO differential image motion monitor

M. Sarazin[1] **and F. Roddier**[2]

[1] European Southern Observatory, Karl-Schwarzschild-Strasse 2, D-8046 Garching bei München, Federal Republic of Germany
[2] Institute for Astronomy, University of Hawaii, 2680 Woodlawn Dr., Honolulu, HI 96822, USA

Received February 27, accepted May 24, 1989

Abstract. The theory of differential image motion measurements is reviewed and the ESO seeing monitor is described. Seeing estimates made with the monitor are found to be in excellent agreement with actual seeing values observed with a large telescope.

Key words: site testing – seeing – earth atmosphere

1. Introduction

Performance of large telescopes is highly dependent upon image quality, and selecting sites with good seeing conditions has become an increasingly important matter. Ideally one would wish a small transportable instrument that would accurately predict the quality of the image a large telescope would produce at the same location. Traditionally, astronomers have relied upon measuring image quality with small telescopes. However, such measurements are often inaccurate. Moreover, on good sites it requires at least a 40 cm telescope with good optics and good tracking accuracy, which makes the instrument hardly transportable.

Image quality is directly related to the statistics of the perturbations of the incoming wavefront, which are now well understood (F. Roddier, 1981). With wavefront sensing methods, wavefront fluctuations can be directly analyzed, providing quantitative information on seeing, independent of the telescope being used. For instance the amplitude of local wavefront tilt errors can be accurately measured with small instruments. As a matter of fact, star trail photographs have long been used to assess image quality (Harlan et al., 1965). Photoelectric image motion monitors, pioneered by Irwin (1966), provide information that can be more easily converted into absolute seeing disk sizes. However, such instruments are sensitive to tracking errors and to the turbulence outerscale (see F. Roddier, 1981, p. 336). Interferometers have been successfully used to measure directly the wavefront coherence, independent of the telescope optics (C. Roddier et al., 1986), but the method is also sensitive to tracking errors and interferometers are delicate to operate in adverse, dusty environments.

Following the advice of one of us (F.R.), the European Southern Observatory (ESO) decided in November 1984 to develop a differential image motion monitor (DIMM). The method consists of measuring wavefront slope differences over two small pupils some distance apart. Because it is a differential method, the technique is inherently insensitive to tracking errors. It had already been used as early as 1960 to provide qualitative seeing estimates (Stock et al., 1960), and later by Miller et al. (1975), with an external calibration. Following ESO, the National Optical Astronomy Observatories (NOAO) switched from absolute to differential image motion measurements for their NNTT site testing campaign (Forbes et al., 1988). The theory of differential measurements is now well understood. It shows that the differential motion exceeds the absolute motion as soon as the distance between the two apertures equals a few times their diameter. Hence a compact instrument can be built and still provide good sensitivity. Moreover, as shown below, the results can be expressed in terms of an absolute seeing scale, using an approximate but still accurate analytical formula.

The theory is reviewed below and the ESO seeing monitor is described. Seeing estimates obtained with this instrument are compared to actual seeing values observed simultaneously with a large telescope.

Send offprint requests to: M. Sarazin

2. Theory

The wavefront corrugation $z(x, y)$ is proportional to the wavefront phase error $\phi(x, y)$:

$$z(x, y) = \frac{\lambda}{2\pi}\phi(x, y). \tag{1}$$

Since light rays are normal to the wavefront surface, the component α of the angle-of-arrival fluctuation in the x direction is given by:

$$\alpha(x, y) = -\frac{\partial}{\partial x} z(x, y) = -\frac{\lambda}{2\pi}\frac{\partial}{\partial x}\phi(x, y). \tag{2}$$

Hence, the covariance of the angle-of-arrival fluctuation:

$$B_\alpha(\xi, \eta) = \langle \alpha(x, y), \alpha(x + \xi, y + \eta) \rangle \tag{3}$$

is related to the covariance $B_\phi(\xi, \eta)$ of the phase fluctuation by

$$B_\alpha(\xi, \eta) = -\frac{\lambda^2}{4\pi^2}\frac{\partial^2}{\partial \xi^2} B_\phi(\xi, \eta). \tag{4}$$

Introducing the phase structure function

$$D_\phi(\xi, \eta) = 2[B_\phi(0, 0) - B_\phi(\xi, \eta)] \tag{5}$$

yields:

$$B_\alpha(\xi,\eta)=\frac{\lambda^2}{8\pi^2}\frac{\partial^2}{\partial\xi^2}D_\phi(\xi,\eta). \tag{6}$$

For Kolmogorov turbulence at the near-field approximation, the phase structure function is given by the widely used expression (1)

$$D_\phi(\xi,\eta)=6.88\left(\frac{r}{r_0}\right)^{5/3} \tag{7}$$

where $r=\sqrt{\xi^2+\eta^2}$ and r_0 is Fried's seeing parameter. Putting (7) into (6) gives:

$$B_\alpha(\xi,\eta)=0.087\,\lambda^2 r_0^{-5/3}\frac{\partial^2}{\partial\xi^2}[\xi^2+\eta^2]^{5/6}$$

$$=0.145\,\lambda^2 r_0^{-5/3}\left[(\xi^2+\eta^2)^{-1/6}-\frac{1}{3}\xi^2(\xi^2+\eta^2)^{-7/6}\right]. \tag{8}$$

For $\eta=0$, we get the longitudinal covariance (in the direction of the tilt) as a function of the separation $\xi=d$:

$$B_l(d)=B_\alpha(d,0)=0.097\left(\frac{\lambda}{r_0}\right)^{5/3}\left(\frac{\lambda}{d}\right)^{1/3}. \tag{9}$$

For $\xi=0$, we get the lateral or transverse covariance (in a direction perpendicular to the tilt) as a function of the separation $\eta=d$:

$$B_t(d)=B_\alpha(0,d)=0.145\left(\frac{\lambda}{r_0}\right)^{5/3}\left(\frac{\lambda}{d}\right)^{1/3}. \tag{10}$$

The transverse covariance is exactly 1.5 times larger than the longitudinal covariance and both decrease as the $-1/3$ power of the separation. This was well confirmed experimentally by Borgnino et al. (1978). These expressions are valid only within the inertial range of the Kolmogorov spectrum. The divergence at the origin is clearly not physical. In practice, the value at the origin is limited by aperture averaging and is given by the expression for the variance of image motion derived by Fried (1965, 1975), and Tatarski (1971), (within a factor of two since we consider motion in one direction only):

$$B_\alpha(0,0)=0.179\left(\frac{\lambda}{r_0}\right)^{5/3}\left(\frac{\lambda}{D}\right)^{1/3} \tag{11}$$

where D is the diameter of the apertures through which tilts are measured. Because of the slow decrease of the covariance as the $-1/3$ power of the distance d in (9) and (10), aperture averaging does not noticeably modify the covariance function as soon as the distance exceeds twice the aperture diameter, as shown below.

The variance $\sigma^2(d)$ of the differential image motion observed over a distance d is given by:

$$\sigma^2(d)=2[B(0)-B(d)]. \tag{12}$$

Putting (9) and (11) into (12) gives an approximate expression for the variance σ_l^2 of the differential longitudinal motion for $d\geq 2D$:

$$\sigma_l^2=2\lambda^2 r_0^{-5/3}[0.179D^{-1/3}-0.0968d^{-1/3}] \tag{13}$$

whereas putting (10) and (11) into (12) gives an approximate expression for the variance σ_t^2 of the differential transverse motion for $d\geq 2D$:

$$\sigma_t^2=2\lambda^2 r_0^{-5/3}[0.179D^{-1/3}-0.145d^{-1/3}]. \tag{14}$$

These variances can be expressed in terms of the total variance for two-dimensional motion through a single aperture of diameter D:

$$\sigma^2=2B_\alpha(0,0)=0.358\left(\frac{\lambda}{r_0}\right)^{5/3}\left(\frac{\lambda}{D}\right)^{1/3}. \tag{15}$$

Putting (15) into (13) and (14) with $S=d/D$ gives:

$$\sigma_l^2=[1-0.541\,S^{-1/3}]\sigma^2, \tag{16}$$

$$\sigma_t^2=[1-0.811\,S^{-1/3}]\sigma^2. \tag{17}$$

Numerical values derived from these expressions have been compared to the results of more extensive calculations made by Fried (1975). According to Fried:

$$\sigma_l^2=I(S,0)\sigma^2 \tag{18}$$

$$\sigma_t^2=I\left(S,\frac{\pi}{2}\right)\sigma^2 \tag{19}$$

where $I(S,0)$ and $I(S,\alpha/2)$ are tabulated in Fried's paper. Table 1 shows a comparison between these tabulated values and the coefficients in (16) and (17). The agreement is expected to improve as S gets larger. Surprisingly, it is best for $S=6.5$ to 7 and degrades at larger S values. We believe this is due to uncertainties in Fried's numerical integration and that our expression is probably more accurate for large S values. For longitudinal motion, all values but the last agree within 4%. For transverse motion, the maximum difference is 17.3% for $S=1$. It is still 7% for $S=2$. Figure 1 shows the rms differential motion predicted by these expressions for two 4 cm apertures 20 cm apart. Full lines are obtained from our expression and dots from Fried's coefficients.

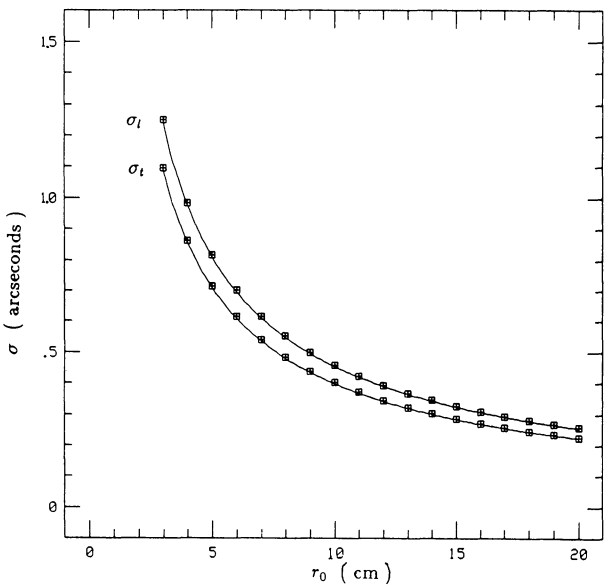

Fig. 1. Theoretical rms longitudinal σ_l and transverse σ_t differential image motion as a function of Fried's r_0 seeing parameter for two 4 cm apertures 20 cm apart. Full lines are given by (13) and (14). Dots are from numerical computations in (Fried, 1975)

Table 1. Relation to two-dimensional motion for various aperture-to-separation ratios

S	$I(S, 0)$			$I(S, \pi/2)$		
	Fried	This paper	% difference	Fried	This paper	% difference
1.0	0.460	0.459	−0.2	0.228	0.189	−17.3
1.5	0.545	0.527	−3.2	0.320	0.291	−9.0
2.0	0.593	0.571	−3.8	0.382	0.356	−6.8
2.5	0.625	0.601	−3.8	0.425	0.402	−5.4
3.0	0.648	0.625	−3.6	0.458	0.437	−4.5
3.5	0.665	0.644	−3.2	0.484	0.466	−3.8
4.0	0.678	0.659	−2.8	0.504	0.489	−3.0
4.5	0.688	0.672	−2.3	0.521	0.509	−2.4
5.0	0.696	0.684	−1.8	0.535	0.525	−1.8
5.5	0.703	0.694	−1.3	0.546	0.540	−1.0
6.0	0.708	0.702	−0.8	0.555	0.553	−0.3
6.5	0.712	0.710	−0.3	0.564	0.565	0.2
7.0	0.717	0.717	0.0	0.573	0.576	0.5
7.5	0.721	0.724	0.4	0.579	0.585	1.1
8.0	0.720	0.730	1.3	0.582	0.594	2.1
8.5	0.720	0.735	2.1	0.585	0.602	3.0
9.0	0.719	0.740	2.9	0.586	0.610	4.1
9.5	0.718	0.745	3.7	0.588	0.617	4.9
10.0	0.717	0.749	4.5	0.588	0.623	6.0

3. System description

The differential image motion monitor (DIMM) is the main element of the instrumentation package developed for the VLT site evaluation campaign. It was first briefly described by Sarazin (1986a), and the first results were presented the same year (Sarazin, 1986b). Three DIMMs are now in routine operation on candidate sites in Chile. They use 35 cm diameter telescopes in the open air on 5 m high towers.

One needs to select the starlight having passed through two circular apertures in the entrance pupil plane (Hartmann holes) so as to obtain dual star images whose relative motion in the image plane represent local wavefront tilts.

Bright stars are tracked two hours east and west of the meridian, at less than 30° from zenith. The measurements are done at a rate of five relative positions per second. The standard deviation of the wavefront tilt differences in the directions parallel and perpendicular to the direction of separation of the sub-pupils is calculated on 200 such short exposures. This corresponds to one statistical estimate of the current seeing every minute.

For more convenience in changing pupil characteristics, the entrance pupil of the telescope is re-imaged behind the Cassegrain focus by means of a collimator as shown in Fig. 2. Various sizes of pupil plane masks can be used according to average seeing quality. This also permits installation of the DIMM at the focus of any telescope with only minor changes.

In the pupil image plane, a roof prism of angle A splits the starlight into two beams corresponding to the two halves of the primary and introduces a symmetrical tilt in the direction parallel to their separation. To create subapertures of diameter D and separation d, a pupil mask is glued on the prism's plane edge. It consists of two holes of diameter γD and separation γd. Where

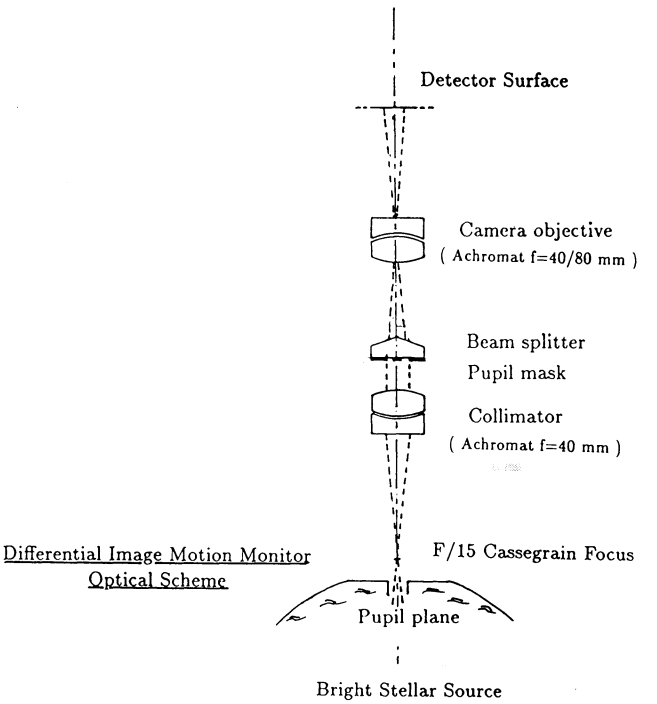

Fig. 2. Optical pupil imaging system

γ is the magnification of the optical system given by:

$$\gamma = \frac{f'}{f}, \tag{20}$$

f is the telescope focal length and f' is the collimator focal length.

The apertures chosen for the VLT site study are 20 cm apart and have a diameter of 4 cm ($S = D/d = 5$). With a 35 cm diameter $f/15$ telescope and a collimator focal length of 4 cm, this corresponds to a pupil mask with two holes of 305 μm diameter at a distance of 1524 μm. When the diameter D of the sub-apertures is smaller than the average Fried parameter r_0 the two images correspond to sightly blurred diffraction patterns. The useful spot diameter, defined as encircling more than 50% of the energy, may then be considered as constant.

The pixel scale is mainly determined by the accuracy required in the determination of the positions of the centroids of the two images. If each spot covers at least 3×3 pixels, the measured error in the determination of the relative positions is given in Sect. 4.2. It corresponds to a variance of 0.01 square pixel. With an aperture of diameter $D = 4$ cm the image width is 3″, this sets a maximum angular scale of 1″ per pixel. As shown in Fig. 1, with such an angular scale and for a separation of 20 cm, 1″ seeing ($r_0 = 10$ cm) creates a relative motion whose variance is 25 times larger than the measurement error.

With the $f/15$, 35 cm diameter telescopes built for the site survey, and the optical arrangement shown in Fig. 2, the detector described below leads to a pixel angular scale of 0.″87. If required in case of exceptionally good seeing conditions (FWHM < 0.″2 at 0.5 μm), it may be reduced by simply exchanging the camera objective.

The choice of the detector is mainly directed by photometric considerations. The bright star population in the zenith area ($\pm 30°$) varies considerably with the location of the tested site as well as with the period of the year. As shown in Table 2, the instrument must be able to work with objects as faint as magnitude $V = 3$–4 so as to be 100% operational. It has been assumed that a star of fifth magnitude provides 100 photons $s^{-1}\,nm^{-1}\,cm^{-2}$. If the detector readout noise is 150 electrons, at least $\times 100$ magnification is necessary to reach a minimum signal-to-noise ratio of 10 for a fourth magnitude star with the 4 cm diameter subapertures.

The detector used in the VLT site study is a microchannel plate image inverter intensifier tube on a 576×384 frame transfer CCD. The tube is equipped with an S 20 photocathode and a P 20 phosphor. No chromatic filter is used since, as shown in Sect. 2, the image motion varies as $\lambda^2 r_0^{-5/3}$ which is independent of the wavelength ($r_0 \propto \lambda^{6/5}$).

Table 2. Number of photoelectrons per pixel as a function of magnitude and of subaperture diameter

Magnitude V	Number of stars in $\pm 30°$ at latitude: -15 to -45 South	Sub-aperature diameter (cm) 4	5	10	20
2	9	117	188	732	2928
3	31	47	74	297	1187
4	62	19	30	119	475
5	154	8	12	48	192

Parameters	
	Optical transmission: 30%
	Quantum efficiency: 20%
	Exposure time: 10 ms
	Wavelength: $\lambda = 550$ nm
	Wavelength band: 200 nm
	Image size (50% energy): 10 pixels

The exposure time is one of the most critical parameters of the measurement and influences the overall accuracy as discussed in greater detail below. We use an electromagnetic shutter to obtain 10 ms exposures. With a cycle frequency of 5 Hz, it is the only expandable part of the whole instrument. Shutter failures are detected automatically by the software. In normal operation (10 hours per night), a shutter has to be replaced approximately every 2 months.

From the CCD frame, only two subarrays of 16×16 pixels are digitized and transferred to the computer through a 16-bit parallel interface. The positions of the two centroids inside the subarrays are determined online after each short exposure. The absolute positions with regard to the CCD are fed back to an autoguiding closed loop to correct for the telescope tracking errors, which allows fully automatic operation.

Each transferred frame undergoes some selection before the centroid determination takes place. Because of the small size of the apertures, the scintillation due to the atmosphere is fairly strong; because of their large separation in the pupil plane, instantaneous intensity levels of the two images are not correlated. Any image containing at least one saturated pixel is rejected. Similarly, if the total illumination in the subarray is under a given threshold, for instance because of temporary cloudiness, the measurement is not taken into account and the loop is resumed.

A dark-field matrix is regularly estimated as the average of several exposures with the shutter closed. The dark-field pixel values are subtracted from the subimages. To keep a rather constant number of pixels in the centroid determination process, an adaptive threshold is defined for each spot as a fraction of its maximum pixel value. All pixels under the threshold are set to zero.

At the end of the fast exposures, the standard deviations of relative motion and intensity are computed. The corresponding values of seeing and scintillation are immediately available to the operator. The index of scintillation $\sigma^2(I)/I^2$ computed from 10 ms exposures corresponds to a cutoff frequency of 50 Hz which is smaller than the cutoff frequency of the atmosphere. The real index is also measured in parallel with a photometer of 1 k Hz bandpass. It is a useful indication of the amount of turbulent activity in the high atmosphere.

4. Data processing

4.1. Introduction

The differential image motion uses a direct measurement method, in the sense that all parameters involved are perfectly measurable and no reference is needed. The main calibration lies in the estimate of instrumental noise and system limitations.

The resolution θ of a large telescope limited by atmospheric turbulence, as defined by the Strehl criterion, is:

$$\theta = (4/\pi)\lambda/r_0. \tag{21}$$

The full width at half maximum (FWHM) of a long exposure stellar image at zenith is the most commonly used parameter. It is related to the Fried seeing parameter via the atmospheric long exposure optical transfer function which, according to F. Roddier

(1981), is given by

$$T(r) = \exp -\frac{D_\phi(r)}{2} \tag{22}$$

where D_ϕ is the phase structure function given in (7). The FWHM of the corresponding point spread function was estimated numerically as a function of wavelength and r_0 using standard software (Dierickx, 1988):

$$\mathrm{FWHM} = 0.98\frac{\lambda}{r_0}. \tag{23}$$

According to the results of Sect. 2, the long exposure image size may be computed from differential motion measurements on a star at zenith distance γ along:

$$\mathrm{FWHM} \propto \lambda^{-1/5}[\sigma_\star^2 \cos\gamma]^{3/5}. \tag{24}$$

The subscript $\star$ represents either of the two directions of measurement, longitudinal and transverse. Since the differential motion is measured independently in both directions, the system delivers two estimates for the image size using the proportionality coefficients given in (13) and (14). This characteristic is extremely helpful, firstly to reduce the statistical error and secondly to check for direction-dependent error factors such as temporal averaging due to finite exposure time.

The FWHM varies as the 6/5 power of the standard deviation of the motion, which is measured in fractions of pixels. An error in the determination of the pixel angular scale induces a 1.2 times larger error in the FWHM. The pixel scale is regularly checked by imaging, with the full aperture of the telescope, optical double stars of known separation. For that purpose, only the pupil mask is removed; the system remains in the same optical configuration (f/15) and the average separation is measured out of multiple exposures. The pixel size is determined with an accuracy better than 1%.

The DIMM measurements are sensitive to three type of errors which are now reviewed in more detail.

4.2. *Instrumental noise*

The uncertainty in the determination of the relative positions of the centroids introduces an error appearing as a noise of standard deviation σ_n which is not correlated with the true motion. If σ_0 is the standard deviation of the apparent motion, the noise must be subtracted out:

$$\sigma_\star^2 = \sigma_{0\star}^2 - \sigma_{n\star}^2, \tag{25}$$

In the case of the differential motion experiment, the detector used has square pixels. The accuracy of the centroid algorithm, measured in the laboratory on two fixed spots, corresponds to an equivalent systematic error in both directions of measurement:

$$\sigma_n^2 = \sigma_{nl}^2 = \sigma_{nt}^2 = 0.01 \pm 0.002(\mathrm{pixel}^2). \tag{26}$$

This value is also valid in the field provided that signal-to-noise ratios with respect to CCD readout noise and photon noise do not change. The intensification level is adjusted for each star automatically so as to keep a constant average illumination on the CCD. The limiting magnitude of the stars is chosen so as to keep the photon noise at an acceptable level (10%). With such precautions, the measurement noise may vary only during periods of strong scintillation, which generally correspond to poor seeing and thus to differential motions much larger than the noise. The error $\delta\sigma_n^2$ in the determination of the measurement noise sets the limit of the system for large r_0. The relative error on seeing measurements after noise subtraction is given by:

$$\frac{\delta\mathrm{FWHM}_\star}{\mathrm{FWHM}_\star} = \frac{3}{5}\frac{\delta\sigma_n^2}{\sigma_\star^2}. \tag{27}$$

The relative instrumental error in both directions of measurement is plotted in Fig. 3 versus r_0 for a pixel angular scale of 0.″87 and at 0.5 μm. A 0.″2 seeing ($r_0 = 50$ cm) is measured with an accuracy of $\pm 5\%$.

4.3. *Statistical errors*

The variance of image motion is obtained from N short exposure images. The N samples are considered statistically independent and the recording time is chosen short enough that the statistical properties of the motion remain constant, i.e., that the distance between the two images follows a normal law. The statistical error on the estimate is then, according to Frieden (1983):

$$\frac{\delta\sigma_\star^2}{\sigma_\star^2} = \sqrt{\frac{2}{N-1}}. \tag{28}$$

The number of samples has to be as large as possible; it is limited by the rate of transfer of the images and the computing time. The short-term stability of the atmosphere is given by the convergence of the standard deviation. For typical conditions, the atmosphere keeps the same statistical properties for about one minute. This gives enough time to record and process $N = 200$ images. The achieved accuracy in terms of image size is then:

$$\frac{\delta\mathrm{FWHM}_l}{\mathrm{FWHM}_l} = \frac{\delta\mathrm{FWHM}_t}{\mathrm{FWHM}_t} = \frac{3}{5}\frac{\delta\sigma_\star^2}{\sigma_\star^2} = 6\%. \tag{29}$$

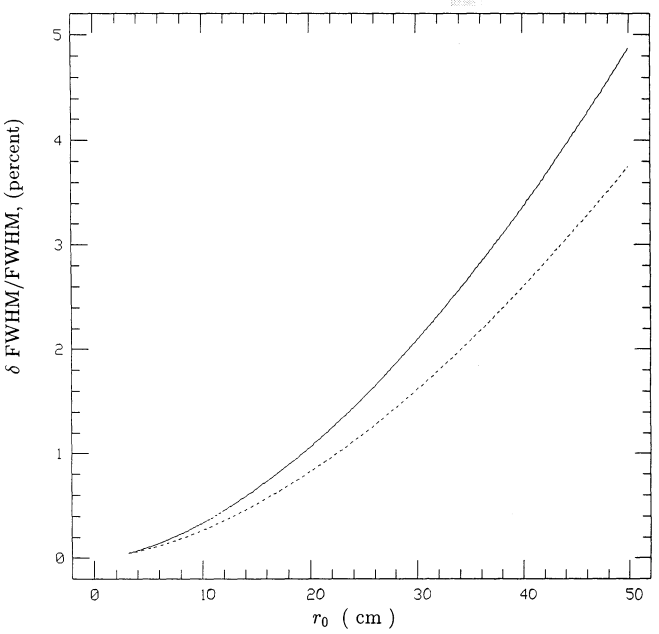

Fig. 3. Relative instrumental error on FWHM measurements from transverse (full line) and longitudinal (broken line) motion versus Fried parameter at 0.5 μm for a pixel angular size of 0.″87

If one plots the results obtained from longitudinal and transverse motion against each other, the impartial slope of the regression line should be equal to 1 with a spread of ± 12%. As shown in Fig. 4, this is verified by 90% of the 735 pairs of measurements obtained during the calibration tests described by Pedersen et al. (1988).

In the absence of direction dependent error, both estimates have the same accuracy, the best estimate of the current image size is given by their average, which brings the final statistical error to ±4.25% for individual results.

4.4. Exposure time

The main drawback of the differential method is the very short exposure time required to freeze the motion in case of turbulence created in regions of the atmosphere with high wind speed.

The effect of wind speed on measured differential motion has been computed by Martin (1987) in the case of one single turbulence layer. It depends on the direction of the motion of the turbulent area with respect to the subaperture separation and the measurement direction. For a given wind speed, the attenuation coefficient

$$\eta_\star = \frac{\sigma^2_\star}{\sigma^2_{0\star}} \tag{30}$$

is closer to 1 for longitudinal motion when the wind is perpendicular to the aperture separation. On a site dominated by jet-stream (west/east) winds, the subaperture separation has to be in north–south direction in order to increase the detectivity for those fast moving layers. Moreover, if one assumes a constant direction of motion for the turbulent layers, it is possible to evaluate this attenuation coefficient from the ratio of attenuation coefficients in each direction of measurement η_l/η_t.

It can be shown that a large correction applied to a small fraction of the total seeing (as in the case of fast, weakly turbulent layers) is very comparable to correcting the whole seeing by a smaller amount as done in the single-layer assumption. An a posteriori correction is thus possible, which in our case never exceeds 10% of the total seeing in a monthly average.

5. Comparison with large telescope seeing

The seeing monitor normally operates in the open air on a 5 m high tower. It was noticed during measurements at La Silla that the DIMM always indicated better seeing than measured at the focus of the large telescopes of the observatory. This could be expected because of additional perturbations inside domes and at the surface of primary mirrors. Yet, no conclusion could be reached on the accuracy of the seeing measurements unless the instrument were operating inside the dome itself.

Two nights were allocated at La Silla on the 2.2 m telescope for the comparison of the differential motion seeing with large telescope seeing, from May 26 to 28, 1988 (Pedersen et al., 1988). The seeing monitor was attached with its 35 cm diameter optics on the side of the 2.2 m primary mirror cell. Both instruments were thus inside the dome, observing the same stars close to zenith position.

Full widths at half maximum (FWHM) of stellar images were measured on 50 s exposures in direct CCD imaging mode on the 2.2 m. Figure 5 shows the comparison during the second night of measurements. The 2.2 m data have been shifted 2″ upwards to help differentiate between the two curves, which otherwise overlap even during events of short temporal scale.

The comparison of DIMM results and 2.2 m data gives a correlation coefficient of 0.97 for the best linear fit as shown in Fig. 6.

6. Conclusion

Our goal was to construct a small transportable instrument able to work in the open air and yet produce quantitative estimates of the image quality that a perfect large telescope would produce at the same location. Clearly, this goal has now been achieved. Several copies of this instrument have been extensively used for the European Very Large Telescope (VLT) site testing campaign, in search of the best possible location for this telescope.

Since this seeing monitor gives reliable estimates of the open air seeing on an absolute scale, one may envisage the use of such

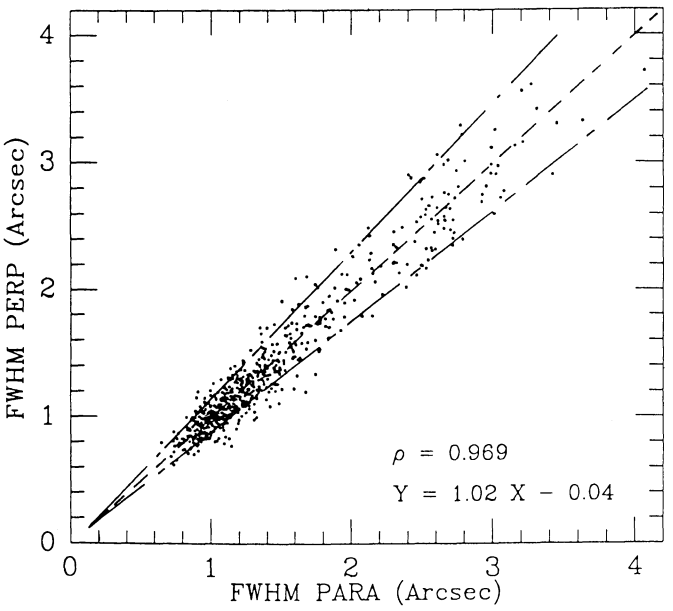

Fig. 4. Regression line between FWHM computed from longitudinal and transverse motion. Dotted lines are $Y=(1\pm0.12)X$

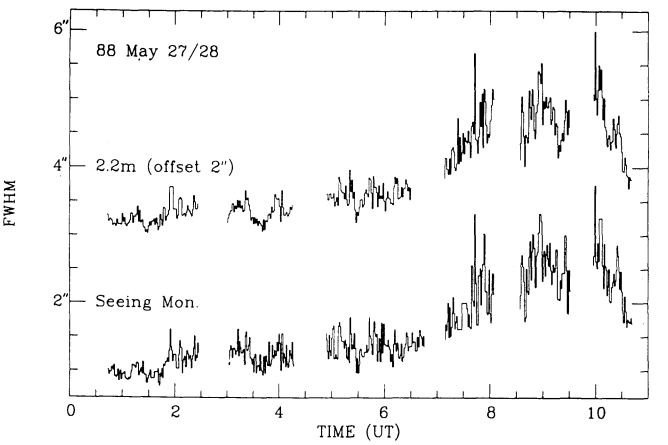

Fig. 5. Comparison of seeing measurements. The 2.2 m data have been offset by + 2″ for clarity

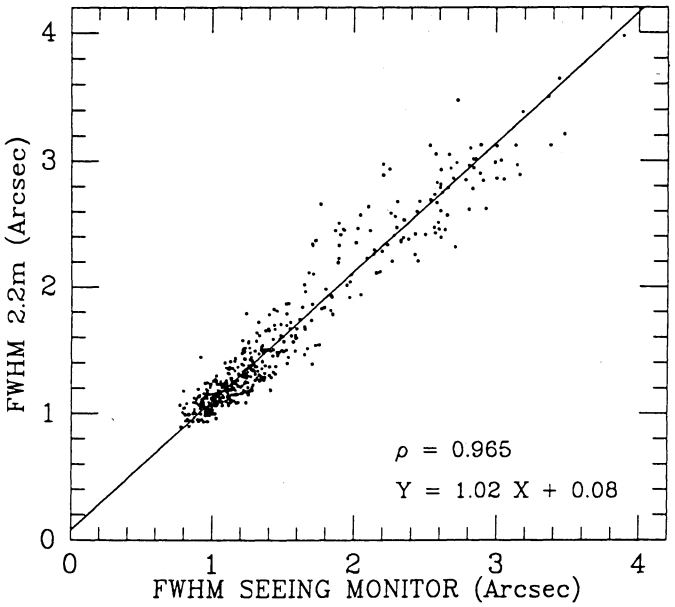

Fig. 6. Correlation coefficient and linear regression for the two nights of intercomparison

instruments permanently outside telescope domes but at the same height above ground. Any difference observed between the seeing measured by the monitor and the telescope would have to be attributed to dome or telescope induced seeing and/or telescope optical aberrations. This could be a powerful diagnostic tool to control and improve image quality of already existing telescopes. Permanent records of the intrinsic seeing quality of an observatory site would also reveal connections between seeing conditions and atmospheric parameters such as wind and temperature distribution. Weather forecasts might then be used to predict seeing conditions, allowing more efficient scheduling of observations.

Acknowledgements. The realisation of the instrument was made possible by the active support of many ESO staff members in Garching and in Chile. We are particularly indebted to M. Cullum, L. Noethe and B. Koehler.

References

Borgnino, J., Vernin, J.: 1978, *J. Opt. Soc. Am.* **55**, 1056

Dierickx, P.: 1988, *IMAQ 0.7, Diffraction Analysis Software Package*, ESO, Nov. 1988

Forbes, F.F., Morse, D.A., Poczulp, G.A.: 1988, *Opt. Eng.* **27**, 845

Fried, D.L.: 1965, *J. Opt. Soc. Am*, **55**, No. 11, 1427

Fried, D.L.: 1975, *Radio Science* **10**, No. 1, 71

Frieden, B.R.: 1983, *Probability, Statistical Optics and Data Testing*, Springer, Berlin, Heidelberg, New York, p. 248

Irwin, J.B.: 1966, *Astron. J.* **71**, 28

Harlan, E.A., Walker, M.F.: 1965, *Publ. Astron. Soc. Pac.* **77**, 246

Martin, H.M.: 1987, *Publ. Astron. Soc. Pac.* **99**, 1360

Miller, M.G., Kellen, P.F.: 1975, *Astronomical Differential, Angle of Arrival Measurement*, Top. Meet. on Imaging in Astronomy, Cambridge, Ma., June 18–21, 1975

Pedersen, H., Rigaut, F., Sarazin, M.: 1988, *The Messenger* **53**, 8

Roddier, C., Roddier, F.: 1987, *Seeing measurements with a pupil-plane rotation shearing interferometer*, Proc. of the Int. Conf. on *Identification, Optimization, and Protection of Optical Sites*, Flagstaff, Arizona, May 22–23, 1986,eds. R.L. Millis et al., Lowell Obs., Flagstaff, p. 58

Roddier, F.: 1981, *The effect of atmospheric turbulence in optical astronomy*, ed. E. Wolf, Progress in Optics, Vol. XIX, p. 281

Sarazin, M.: 1986a, *ESO-VLT Instrumentation for site evaluation in Northern Chile*, SPIE, Vol. 628, Advanced Technology Optical Telescopes III, March 1986

Sarazin, M.: 1986b, *ESO-VLT site evaluation II*, Nov. 86, Proc. Second Workshop on ESO's Very Large Telescope, Venice, 29 Sept.–2 Oct 1986

Stock, J., Keller, G.: 1960, *Astronomical Seeing*, in *Stars and Stellar Systems*, eds. G.P. Kuiper, B.M. Middlehurst, Vol. 1, Chicago University Press, Chicago, p. 138

Tatarski, V.I.: 1971, *The effect of Turbulent Atmosphere on Wave Propagation*, I.P.S.T., Jerusalem